Squeezed Light in a Cryogenic Optomechanical System

Clara Ursic*
Rice University, Houston, TX

Pierre-Édouard Jacquet, Pierre-François Cohadon
Laboratoire Kastler-Brossel, Sorbonne Université UPMC, Jussieu, Paris, France

(Dated: September 18, 2023)

Frequency-dependent squeezed states are quantum states of light that allow measurements to beat the Standard Quantum Limit, providing sensitivity improvements to gravitational wave interferometers and improving optomechanics and quantum computing experiments. LKB's frequency-dependent squeezed light (FDSL) generator and phononic crystal membrane experiment were optimized, with the goal of eventually combining the two experiments into a larger FDSL cryogenic optomechanical system.

* cfu1@rice.edu

I. BACKGROUND

A. Gravitational Wave Interferometry

Gravitational waves were first predicted by Albert Einstein in 1916 as "ripples" in space-time due to violent, energetic processes. The General Theory of Relativity asserts that massive astrophysical events—colliding neutron stars, orbiting black holes, or supernovae—would disrupt space-time, causing waves of undulating space-time traveling at the speed of light to propagate in all directions [17]. Einstein's prediction was confirmed in September 2015 with the first detection of gravitational waves by the Laser Interferometer Gravitational-wave Observatory (LIGO) in Hanford, Washington and Livingston, Louisiana. Since this first detection, the field of gravitational wave astronomy has grown tremendously, with efforts made to improve the sensitivity of gravitational wave interferometers, shown in Figure 1 below. Sensitivity improvements increase the range of detectors, enabling the detection of weaker signals from farther away sources.

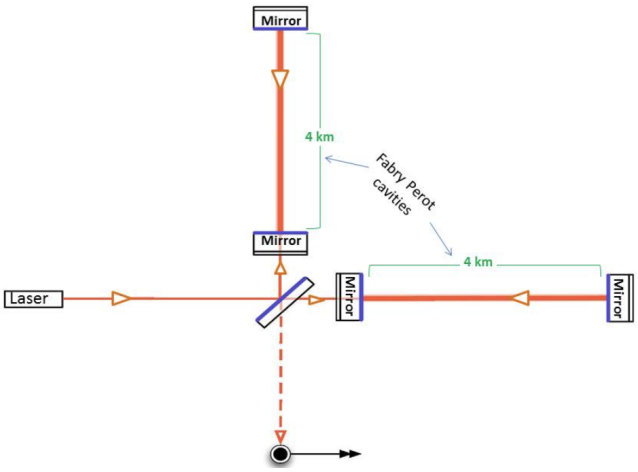

FIG. 1: Simplified Gravitational Wave Detector: Michelson Interferometer with 4 Km Fabry-Perot Cavities [17].

B. Noise

Interferometric measurements of mechanical displacements in LIGO are limited by a plethora of different noise sources, as shown in Figure 2 to the right.

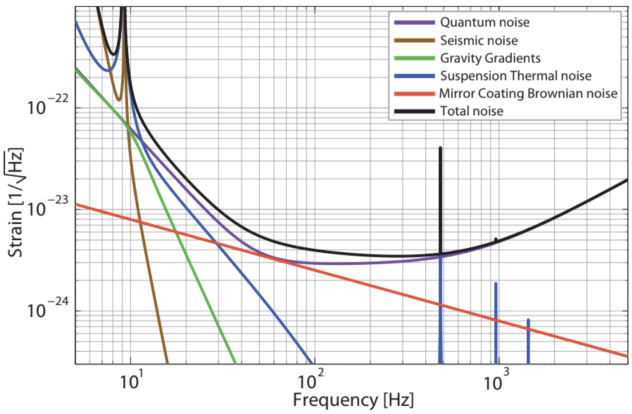

FIG. 2: Noise Limitations in Advanced LIGO [5].

Interferometers' quantum noise, the purple curve, is investigated via tabletop optomechanics experiments at the Laboratoire Kastler-Brossel (LKB). There are two kinds of quantum noises or uncertainties that are specific to a laser interferometer: Quantum Shot Noise (QSN) and Quantum Radiation Pressure Noise (QRPN). They are consequences of the random fluctuations in the arrival time of photons, or in other words, fluctuations in the modulus and phase of the electromagnetic (EM) field. QSN is caused by fluctuations in the phase of the EM field, which introduces uncertainty at the detector. QRPN is caused by fluctuations in the amplitude of the EM field landing on the interferometer's test masses, which induces a mechanical jitter of the masses via radiation pressure [1][5].

The sum of these two quantum noises is minimal at an intermediate laser power, as shown in Figure 3 below, thus enforcing a fundamental limit called the Standard Quantum Limit (SQL). The SQL is the lowest achievable quantum noise for interferometric measurements of mechanical displacements [9][27].

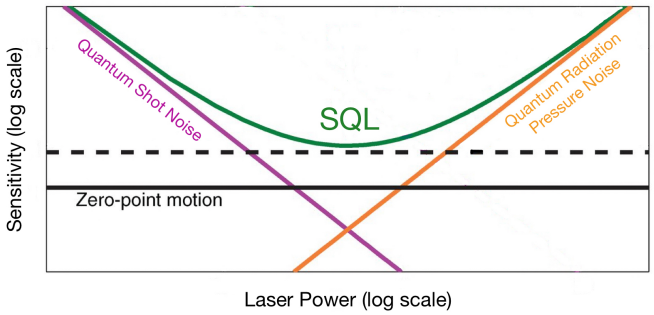

FIG. 3: QSN and QRPN as a Function of Laser Power; Their Intersection Defines the SQL [27].

C. Fabry-Perot Formalism and Optomechanics

To understand the architecture of gravitational wave detectors as well as the tabletop experiments done to study and improve their sensitivities, it is crucial to understand Fabry-Perot optical cavities and optomechanics.

Optomechanics is a newly emerging field focusing on the interaction between light and mechanical resonators. Incoming photon flux landing on a surface transfers momentum to that surface in the form of radiation pressure. The radiation pressure force F_{rad} is proportional to the intensity of the EM field $|\alpha|^2$ by the radiation pressure coupling term κ as shown by Equation 1 below [5].

$$F_{rad} = 2\hbar\kappa|\alpha|^2 \tag{1}$$

Optomechanical coupling occurs when that surface is a mechanical resonator within an optical cavity. The intracavity power depends on the cavity length which in turn depends on the mechanical response to the radiation pressure, which is proportional to the intracavity power. Thus, a closed loop is formed where light drives the motion of the mechanical resonator which then varies the intensity of the light [9]. This coupling is characterized by the mechanical susceptibility χ of the resonator which is a measure of how prone the resonator is to movement by light. Position fluctuations δx_{rad} are proportional to radiation pressure force fluctuations δF_{rad} by χ as shown by Equation 2 below, which of course is all dependent on the particular mechanical frequency Ω [5].

$$\delta x_{rad}[\Omega] = \chi[\Omega]\delta F_{rad}[\Omega] \tag{2}$$

Mirrors in Fabry-Perot cavities, and thus in gravitational wave interferometers, move due to the radiation pressure force of light. We model this coupling with a mirror fixed to a spring, as shown in Figure 4 below. This description is valid close to the resonant frequencies, where only one vibration mode matters, and far from all resonances, where all modes contribute equally. All optical experiments at LKB, as well as gravitational wave interferometers, use very reflective mirrors to achieve high-finesse optical cavities [14].

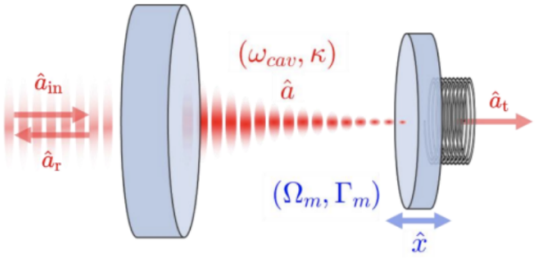

FIG. 4: Optomechanical Coupling Between Laser Light at Optical Frequency ω_{cav} and Mirror at Mechanical Frequency Ω_m [14].

D. Squeezed Light

An effective technique to overcome the Standard Quantum Limit (SQL), and therefore make even more sensitive interferometric measurements, is by inputting nonclassical states of light into the optical cavities of gravitational wave detectors.

An optical cavity is an optomechanical system—a system that couples light to mechanical oscillation—so the Hamiltonian representing the total energy of the EM field in a cavity takes the form of an ensemble of quantum simple harmonic oscillators

$$\hat{H} = \sum \frac{P^2}{2m} + \frac{m\omega^2}{2}x^2 = \sum (\hat{a}^\dagger\hat{a} + \frac{1}{2})\hbar\omega \tag{3}$$

where ω is the optical frequency and $\hat{a}$ and $\hat{a}^\dagger$ are the boson creation and annihilation operators

$$\hat{a}^\dagger = \sqrt{\frac{m\omega}{2\hbar}}(x - \frac{ip}{m\omega}) \qquad \hat{a} = \sqrt{\frac{m\omega}{2\hbar}}(x + \frac{ip}{m\omega}) \tag{4}$$

whose sum are the number operator $\hat{N} = \hat{a}\hat{a}^\dagger$, describing the number of photons in an eigenmode [5].

Light is both a wave and a quantized particle and can be written as a complex exponential visualized in phase space, as seen in Figure 5 on the following page. The X and Y axes refer to the real and imaginary components of the complex amplitude of the EM field, and also to the amplitude and phase quadratures $\hat{X}_2$ and $\hat{X}_1$ respectively (or X and P depending on convention). These quadrature operators are defined by $\hat{a}$ and $\hat{a}^\dagger$:

$$\hat{X}_1 = \hat{a} + \hat{a}^\dagger \qquad \hat{X}_2 = i(\hat{a} - \hat{a}^\dagger) \tag{5}$$

A linear combination of $\hat{X}_1$ and $\hat{X}_2$ describes an arbitrary quadrature in phase space as shown by Equations 6 and 7 below [5].

$$\hat{X}_\phi = \hat{a}e^{-i\phi} - \hat{a}^{i\phi} \tag{6}$$

$$= \hat{X}_1 cos(\phi) + \hat{X}_2 sin(\phi) \tag{7}$$

Due to quantum uncertainty, a beam of light consists of a superposition of phasors, each one representing different possible amplitudes and phases of that light. The radius of the circle on phase space, as shown in Figure 5, represents a distribution of quasiprobability which can also be represented in three dimensions in a Wigner diagram. The darker purple at the center signifies higher probability and the fainter purple at the edges signifies lower probability [5][13].

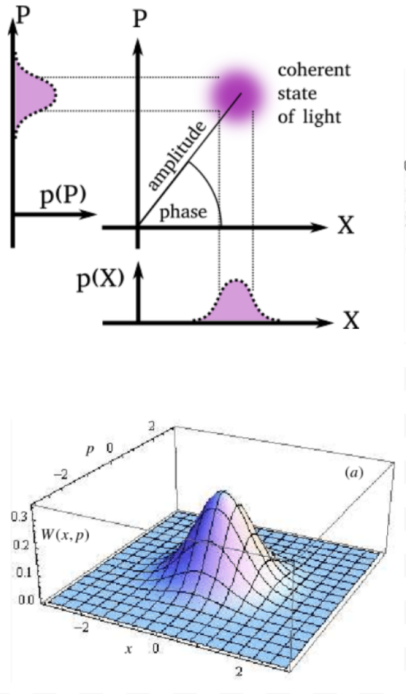

FIG. 5: Phase Space of a Light Source and Accompanying Wigner Diagram [13].

$\hat{X}_1$ and $\hat{X}_2$, or P and X, are Hermitian operators, so represent physically observable quantities. They do not commute, however, so they cannot be simultaneously measured with precise certainty [5].

$$[\hat{X}_1, \hat{X}_2] = 2i \tag{8}$$

The Heisenberg uncertainty principle states that for two noncommuting observables,

$$\Delta\hat{X}_1 \Delta\hat{X}_2 \geq 1 \tag{9}$$

Squeezed light entails modifying the shape of the light on phase space so that there is more certainty in either the amplitude or phase quadrature. Due to the Heisenberg relation, when decreasing uncertainty in one quadrature, there is an unavoidable increase in uncertainty in the other quadrature. This results in a phase diagram where the coherent circle of quantum uncertainty has become ovular, as shown in Figure 6 to the right [5][9].

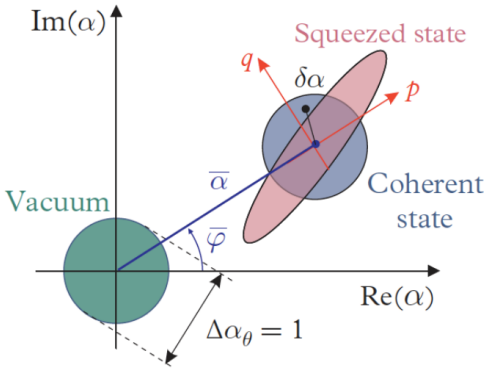

FIG. 6: Phase Space of a Vacuum State, a Coherent State, and a Squeezed State of Light [14].

Light can be squeezed in any direction on the phase space. Squeezing along the q vector, or phase, is called phase squeezing, and results in an increase in certainty of the phase of the light. Squeezing along the p vector, or amplitude, is called amplitude squeezing, and results in an increase in certainty of the amplitude of the light [5][9]. These are shown in Figure 7 below.

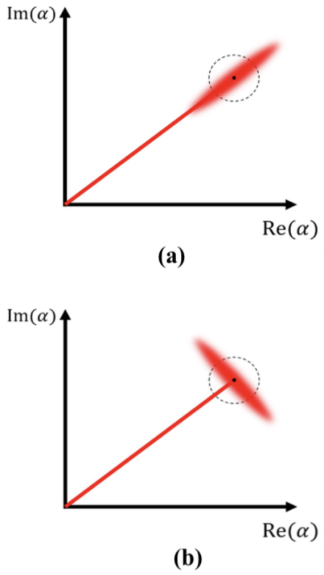

FIG. 7: (a) Phase Squeezing and (b) Amplitude Squeezing [14].

Squeezed states are able to reduce the quantum noise in optical setups to below the SQL, providing sensitivity improvements to gravitational wave interferometers and even improving optomechanics and quantum computing experiments. The injection of squeezed states in advanced LIGO, for example, has already greatly improved detector sensitivity, increasing the binary black-hole detection rate by 50% [19].

E. Frequency-Dependent Squeezing

Frequency-dependent squeezed light (FDSL) refers to changing the squeezing angle of the light based on the light's frequency. QRPN is maximum at the resonant frequency of the optical cavity or mechanical resonator. QSN is frequency independent, so when QRPN lessens outside of the resonator's bandwidth, QSN dominates. For gravitational wave interferometers specifically, whose suspension mirrors typically have a low resonant frequency of about 1 Hz, QRPN dominates at low frequencies while QSN dominates at high frequencies [5]. This is shown in Figure 8 below.

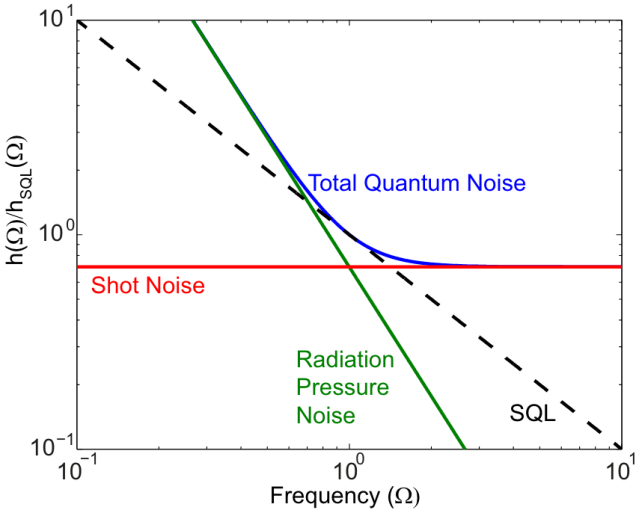

FIG. 8: Frequency Dependence of Quantum Noise in Michelson Interferometer [5].

To simultaneously reduce QRPN at low frequencies and QSN at high frequencies, FDSL is necessary. The angle of the squeezing ellipse is rotated in phase space depending on the frequency of the light. At low frequencies, amplitude squeezing is best to reduce the dominant QRPN, and at high frequencies, phase squeezing is best to reduce the dominant QSN [5]. Frequency-dependent squeezing allows the SQL to be surpassed at a wider range of optical frequencies.

In 2020, LIGO researchers generated FDSL in the frequency range of interest for gravitational wave detection, as shown in Figure 9 on the following page. The colors represent various squeezing angles, the black line shows the minimum quantum noise possible in an interferometer using FDSL, and the grey curve shows a comparison to the injection of frequency-independent squeezed light.

Current upgrades to gravitational wave detectors, like the A+ LIGO upgrade and Advanced VIRGO Plus, involve installing FDSL sources to benefit from broadband, sub-SQL noise reduction [19].

II. EXPERIMENTAL METHODS

LKB's experiment is twofold, with the goal of eventual combination. First, there is the squeezing experiment: designing a tabletop frequency-dependent squeezed light generator. Then there is the membrane experiment: injecting light inside an optomechanical cavity containing a silicon nitride phononic crystal membrane. Once these two experiments are optimized, they will be combined as shown in Figure 10 below. FDSL will be generated and then sent via optical fibers inside a vacuum tank within a cryostat that contains the optomechanical membrane experiment, hence the title "squeezed light in a cryogenic optomechanical system". With such a setup, the goal is to demonstrate how the SQL can be beaten, which has applications in interferometry, quantum computing, weak force sensing like atomic force microscopy, and more.

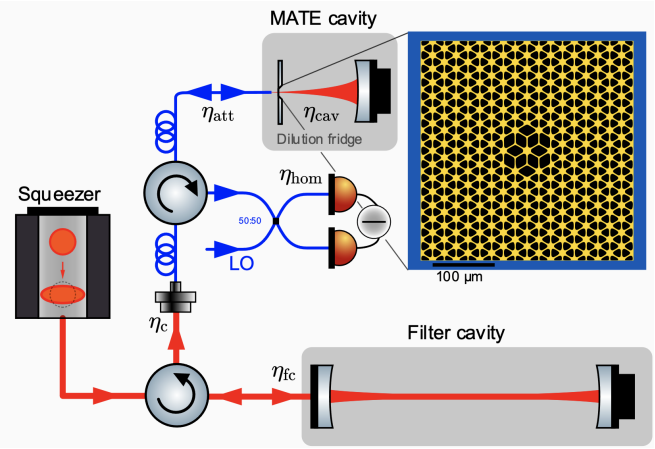

FIG. 10: Future Experiment Combining Optimized Subexperiments [14].

Relevant experimental methods are detailed in this section. First, understanding Gaussian optics is essential to mode match the cavities. Then, using tabletop optical equipment, squeezed light and frequency-dependent squeezed light can be generated. Finally, coupling membranes to optical cavities is of interest in optomechanics experiments.

A. Gaussian Optics and Mode Matching

Laser beams propagate according to a Gaussian profile. If we intersect a laser beam, we find that each transverse beam cross-section has an optical intensity profile described by a Gaussian function [9].

However, if the shape of the incoming Gaussian beam does not match the intrinsic shape of the optical cavity it enters, higher-order, non-Gaussian modes arise. Mode matching is the act of matching the shape of the beam to

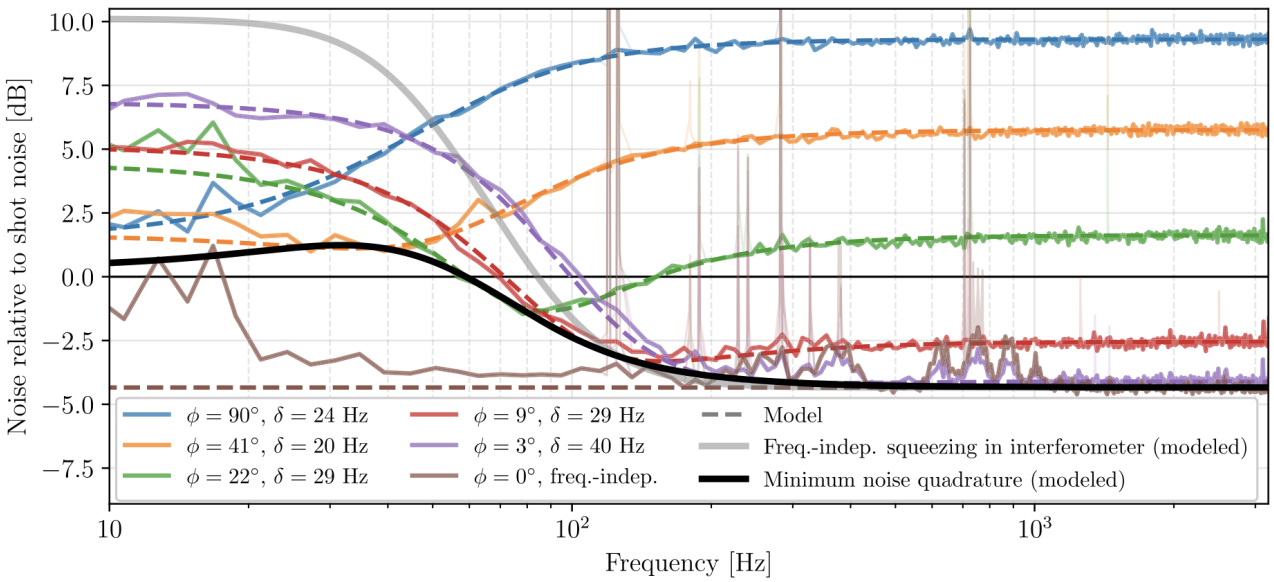

FIG. 9: Frequency-Dependent Squeezing at LIGO Frequencies [19].

the shape of the cavity and is done using lenses, which alter the beam curvature. Through mode matching, we can attain the fundamental TEM 00 Gaussian mode. TEM 00 is the preferred mode for optics experiments as it can be easily focused into a concentrated spot, something incredibly difficult to do with higher-order modes. A concentrated spot is necessary for beams landing on photodiodes or entering devices like the OPO.

B. How Squeezed Light is Generated

To generate squeezed light, the carrier light field is modulated by an external time-varying waveform in either phase or amplitude to produce correlated sidebands.

We start with a complex exponential describing the carrier field.

$$E(t) = E_0 e^{i\omega_0 t} \tag{10}$$

Introducing a periodic amplitude modulation would result in

$$E_{A-Mod}(t) = E_0 e^{i\omega_0 t}(1 + Mcos(\omega_m t)) \tag{11}$$

$$\approx E_0 e^{i\omega_0 t}(1 + \frac{M}{2}e^{i\omega_m t} + \frac{M}{2}e^{-i\omega_m t}) \tag{12}$$

where M is the modulation depth and ω_m is the modulation frequency. Thus, an amplitude-modulated field is decomposed into a carrier and two sidebands at frequencies $\omega_0 \pm \omega_m$. This is shown in Figure 11 (a1) to the right, where the chosen reference is the rotating frame of the carrier at ω_0, and the two sidebands rotate in opposite directions around it [5].

A phase modulation works similarly, resulting in

$$E_{P-Mod}(t) = E_0 e^{i(\omega_0 t + Mcos(\omega_m t))} \tag{13}$$

$$\approx E_0 e^{i\omega_0 t}(1 + iMcos(\omega_m t)) \tag{14}$$

$$\approx E_0 e^{i\omega_0 t}(1 + i\frac{M}{2}e^{i\omega_m t} + i\frac{M}{2}e^{-i\omega_m t}) \tag{15}$$

The result is identical, except the sidebands are shifted by $\frac{\pi}{2}$ from the carrier frequency, as shown in Figure 11 (a2) below.

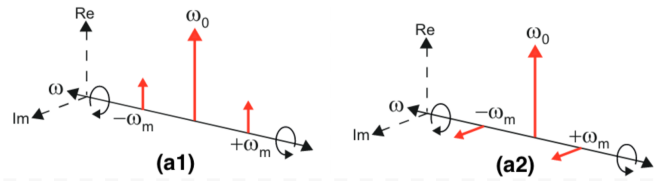

FIG. 11: Sideband Diagram for (a1) Amplitude and (a2) Phase Modulation [5].

The time evolution of the modulation sidebands gives rise to the squeezed light phasor diagram. As time passes, the sidebands rotate in their respective directions in phase space given by the sign of their angular frequency. Summing the carrier and sideband vectors results in the classical phasor evolution, shown in Figure 12 on the following page. For amplitude modulation, 12 (a1), the light changes only along the real axis, so results in a fluctuating amplitude α. For phase modulation, 12 (a2), the light changes only along the imaginary axis, so results in a fluctuating phase ϕ [5].

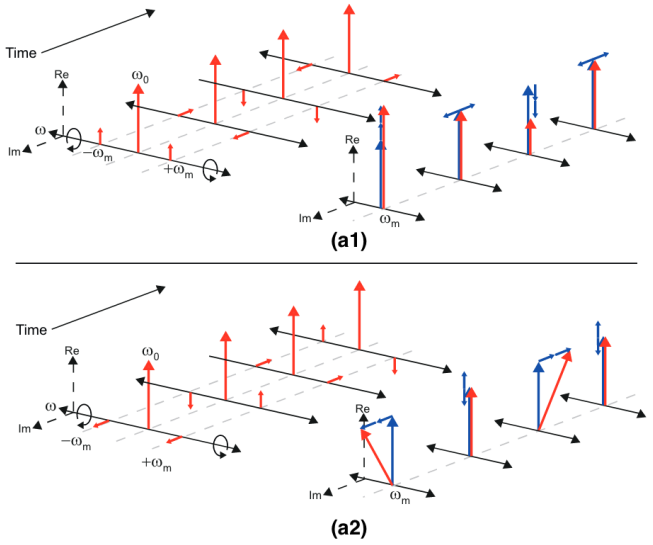

FIG. 12: Time Evolution of Modulation Sidebands with Resulting Phasor Evolution for (a1) Amplitude Modulation and (a2) Phase Modulation [5].

Adding the ball of quantum uncertainty to the tip of the phasors results in a quantum sideband diagram, which traces out the familiar phasor diagram of squeezed states shown in Figure 13 below [5].

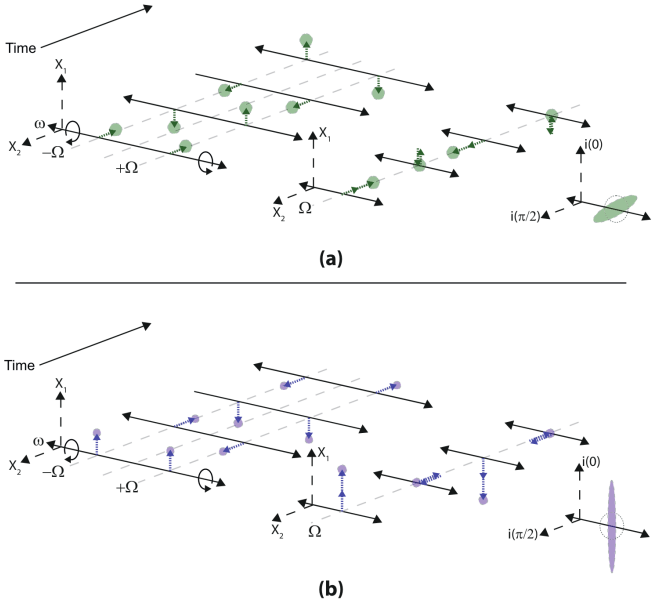

FIG. 13: Time Evolution of Correlated Sidebands with Resulting Phasor Diagram for (a) Amplitude Squeezed and (b) Phase Squeezed Vacuum States [5].

The magnitude of squeezing is determined by how well the sideband pairs are correlated. A strong correlation—meaning a small quantum uncertainty distribution and larger sidebands—results in a more elongated squeezing ellipse. In Figure 13, (b) is more squeezed than (a).

Experimentally, squeezed light is generated by an Optical Parametric Oscillator (OPO). An OPO induces phase or amplitude modulation to create the sidebands and converts each higher-frequency photon into two lower-frequency photons using a nonlinear crystal as shown in Figure 14 below.

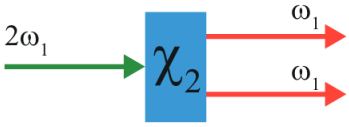

FIG. 14: Optical Parametric Oscillator [5].

Each pair of outgoing photons is entangled, which means the sidebands are correlated. In Figure 11, for example, if the sideband at $\omega_0 + \omega_m$ rotates, the one at $\omega_0 - \omega_m$ rotates too; if the sideband at $\omega_0 + 2\omega_m$, the one at $\omega_0 - 2\omega_m$ rotates too; and so on.

C. How Frequency-Dependent Squeezed Light is Generated

To achieve frequency-dependent squeezing, frequency-independent squeezed light generated by the OPO is injected into a filter cavity. The filter cavity is locked off-resonance with the light carrier frequency—a process called laser detuning—which is shown in Figure 15 below.

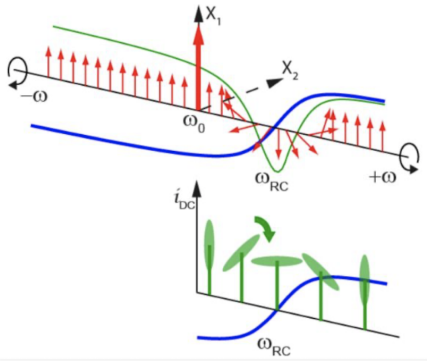

FIG. 15: Carrier Sideband Picture of Frequency-Dependent Squeezing [6].

The blue curve depicts how the phase of the filter cavity changes with respect to frequency: at the cavity's resonant frequency ω_{RC}, constructive interference occurs meaning there is 0 phase difference between transmitted light waves. Shifting the phase response so that resonance does not occur at the carrier frequency ω_0, rather at an upper sideband, causes that sideband to be phase shifted by π (upon reflection in an optical cavity, light experiences a π phase shift), whereas its entangled lower

sideband pair does not get phase shifted. Since the superposition of each sideband pair results in the phase space depiction, the filter cavity serves to rotate the angle of squeezing for sideband frequencies within the cavity linewidth. The magnitude of laser detuning determines the frequency dependence of the squeezing angle [6].

Putting this all together, a simplified FDSL source is shown in Figure 16 below. An infrared laser inputs coherent light into an SHG which generates the green pump for the OPO. The OPO generates correlated sidebands, thus outputting frequency-independent vacuum squeezed light which is then combined with an IR bright field to produce frequency-independent squeezed light, represented by the yellow oval. This then enters the filter cavity and becomes frequency-dependent squeezed light, represented by the tilted pink oval.

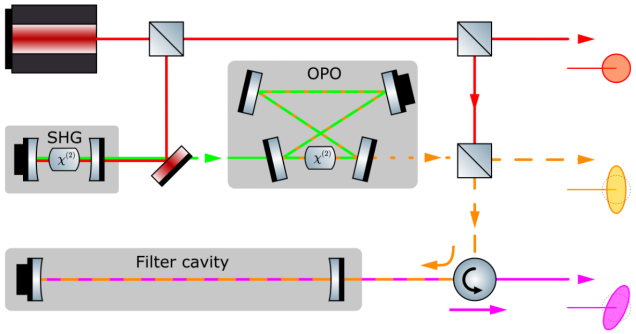

FIG. 16: Simplified FDSL Generation [14].

D. Optomechanical Cavity Membranes

Inserting mechanical intermediaries, such as quartz micropillars or thin silicon nitride membranes, into optical cavities has become increasingly popular in optomechanics research [9]. The interaction between light and the motion of these mechanical resonators allows us to better understand radiation pressure effects, to map the membrane's mechanical modes, and to study the factors that define mechanical damping to the environment.

A particularly promising mechanical resonator is the phononic crystal membrane which is made of a tensioned thin film of silicon nitride (SiN) that is nanopatterned with a central defect. This membrane pattern creates a phononic lattice: a periodic matrix of scatterers. This arrangement of scatterers is advantageous because it creates phononic band gaps, which means the membrane prohibits the propagation of mechanical oscillations in certain frequency ranges. What's more, the oscillations are isolated in the membrane's central defect, which limits its mechanical losses at the edges and allows for longer oscillation lifetimes. A phononic crystal membrane design, mechanical bandgap, and out-of-plane mechanical modes of displacement are shown in Figure 17 to the right.

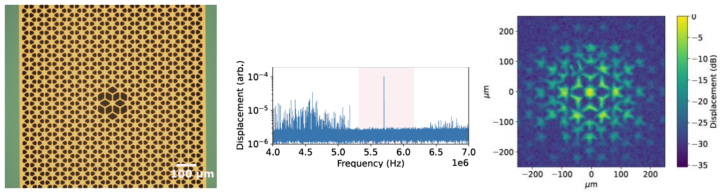

FIG. 17: Phononic Crystal Membrane Mechanical Bandgap and Modes [14].

III. SQUEEZING EXPERIMENT

A. Experimental Setup

The first experiment at LKB is the construction of a tabletop frequency-dependent squeezer. It has successfully produced FDSL in the past, but we are optimizing it to reduce losses. The setup is shown in Figure 18 below. It is slightly more complicated than the one in Figure 16, employing EOMs which lock the optical cavities and a mode cleaner which attenuates higher-order modes.

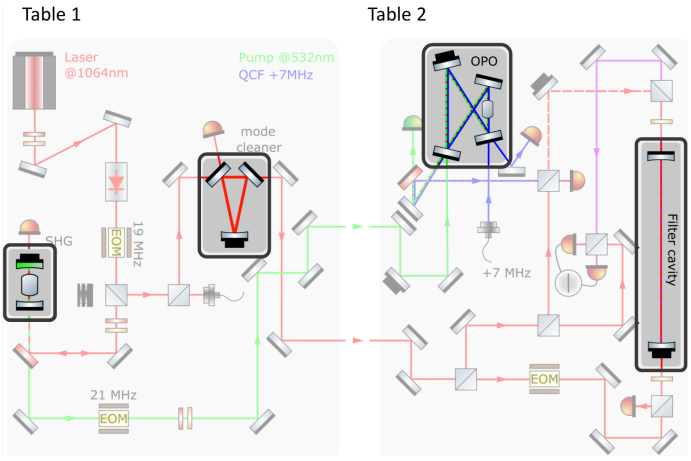

FIG. 18: LKB's Frequency-Dependent Squeezer [14].

B. SHG Alignment and Characterization

This summer, we optimized the beam's path through the SHG. To do this, we mode matched the TEM 00 modes of both the IR ($\lambda = 1064$) and green ($\lambda = 532$) light to the SHG cavity. If the IR beam is not mode matched, the SHG input loses power, and if the green beam is not mode matched, higher-order modes would be sent into the OPO, prohibiting it from functioning. Mode matching the SHG is complicated, however, because the nonlinear crystal inside the cavity slightly changes the cavity mode, as shown in Figure 19 on the following page. The incoming IR light enters the cavity first, so it must be matched to the mode of the cavity *without* the crystal. The green light, which is produced by the crystal, must

be matched to the mode of the cavity *with* the crystal.

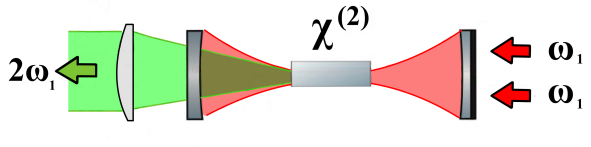

FIG. 19: Second Harmonic Generation Cavity Geometry. Adapted from [15].

To do this, we first removed the crystal and mode matched the cavity to the IR light by changing the orientations of the input mirrors while sweeping the cavity length and observing the real-time transmission response on the oscilloscope. The goal was to maximize the intensity of the TEM 00 fundamental modes with respect to the higher-order modes. Upon optimization, we calibrated and locked the cavity. Figure 20 below shows the oscilloscope reading of the IR input beam after being mode matched. The higher-order modes are of much smaller intensity—in fact, they are barely discernible—compared to the tall Lorentzian resonance peaks of the fundamental mode. The blue curve is the time-varying voltage ramp sent to the piezoelectric actuator that sweeps the cavity length back and forth.

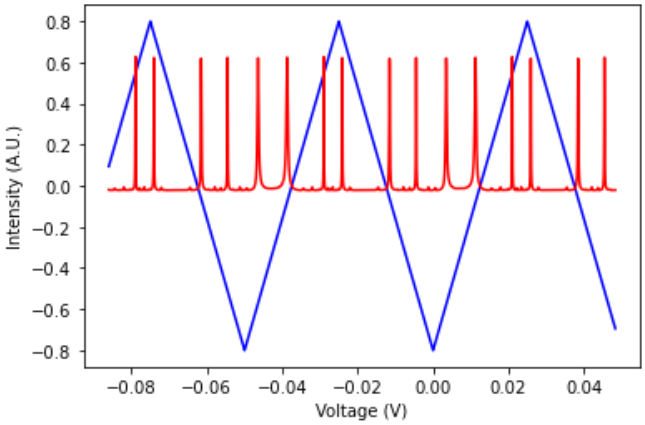

FIG. 20: Resonance Peaks of IR Input Beam in SHG.

Next, we placed the crystal back into the SHG cavity. To see the green beam's cross-section, we placed a camera at the output of the SHG. We then slightly translated and tilted the crystal in order to match the cavity mode to the green beam's TEM 00 mode, visually adjusting to achieve a bright, clean circle of light on the camera. To be able to precisely adjust the crystal position, we designed and 3D printed a custom crystal mount shown in Figure 22 (a) to the right. A cylindrical Thorlabs crystal holder was affixed to the plastic mount, and the dials allowed tilting in two degrees of freedom.

Finally, once both the IR and green beams were aligned and mode matched, we obtained the SHG's conversion efficiency, shown in Figure 21 below. This was done by plotting the power of the IR beam on the X axis and the power of the green beam on the Y axis. Their ratio, the slope, is the amount of IR photons that are converted into green photons. The linear fit has a slope of 0.543, meaning the SHG's efficiency is 54.3%, which is sufficient for squeezing experiments [4].

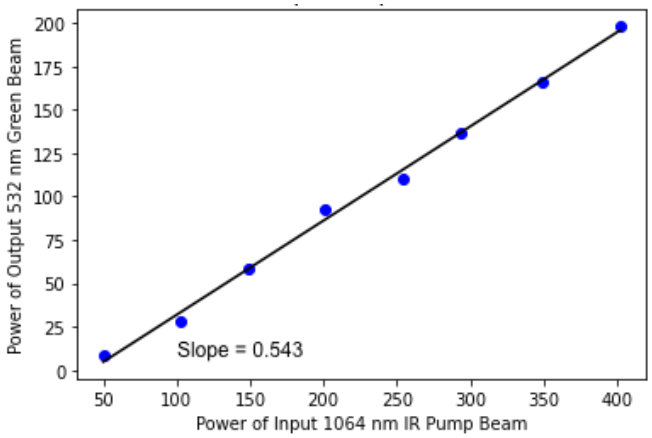

FIG. 21: Conversion Efficiency of IR to Green Light in SHG.

Finally, we designed and machined a copper crystal holder for the OPO as shown in Figure 22 (b) below. The crystal fits inside the rectangular gap and is surrounded on all sides by metal to reduce temperature fluctuations from the environment. This holder was then mounted and placed inside the OPO cavity.

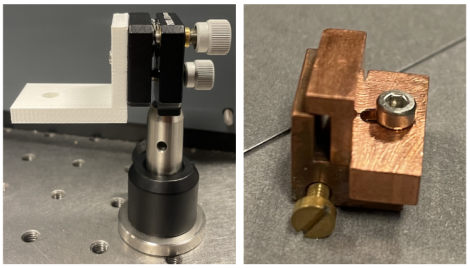

FIG. 22: (a) Custom 3D Printed Nonlinear Crystal Mount for SHG and (b) Custom Copper Nonlinear Crystal Holder for OPO.

C. Future Work and Applications

The next steps are to align, mode match, and lock the OPO, mode cleaner, and filter cavity, which may require further engineering of mounts or other components. Then we can get a final reading of squeezed light. Using a homodyne oscillator, we would sweep through various quadrature angles in phase space and measure the noise

spectra. This requires the optical phase at the homodyne beamsplitter to be controllable at arbitrary phase angles, which is achieved with an electronic control loop. Coherent light is a symmetrical quantum noise distribution, so it would appear as a flat line at or above the SQL line, while squeezed light would oscillate above and below the SQL line, showing squeezing and anti squeezing. An example of this is shown in Figure 23 below.

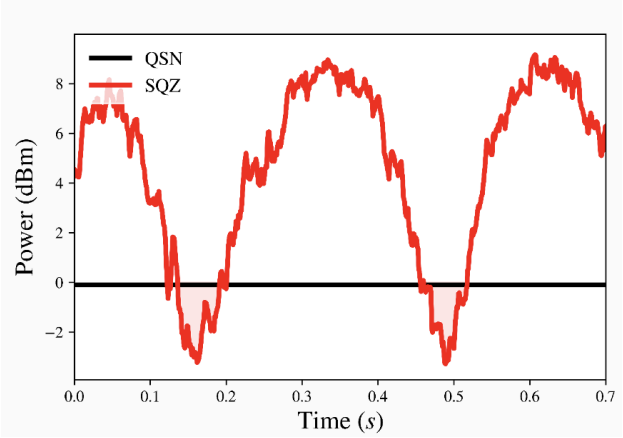

FIG. 23: Measurement of Frequency-Independent Squeezing [14].

For frequency-dependent squeezed light, measurements in different quadrature angles in phase space via homodyne detection would yield different spectra, but noise would always vary with optical frequency. An example of this is shown in Figure 24 below.

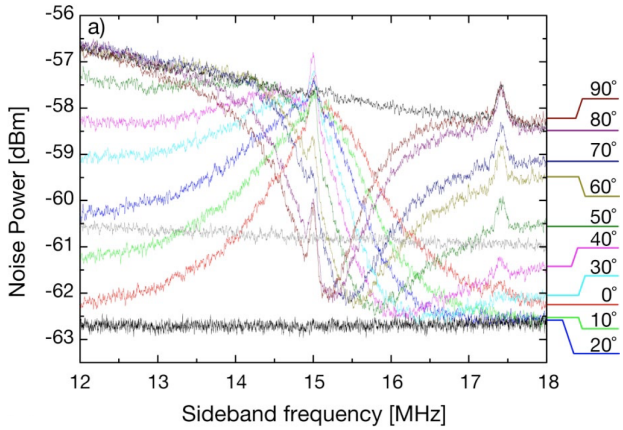

FIG. 24: Measurement of Frequency-Dependent Squeezing for Laser Detuning of $\omega = 15.15$ MHz at Different Quadrature Angles [4].

The grey horizontal line represents the shot-noise limit, measured by blocking the squeezed beam. The graph is bounded by traces of frequency-independent squeezing (lower black line) and anti-squeezing (upper black line). It can be seen that squeezing degrades at high frequencies since the sidebands are no longer within the bandwidth of the OPO cavity.

Developing a tabletop frequency-dependent squeezed light generator is an important proof of concept, a way to study and optimize the setup before applying it on a large scale to gravitational wave interferometers. FDSL generators also serve as a pump for optomechanical and quantum computing experiments, which will be discussed in Section IV next.

IV. MEMBRANE EXPERIMENT

A. Experimental Setup

Next is the membrane experiment, an optomechanics experiment that demonstrates another application of beating the SQL. We aim to map the membrane's mechanical modes, find the ideal phononic crystal membrane design, and optimize membrane fabrication.

The experimental setup and hardware are shown in Figure 25 below. The membrane is held on all sides by a square metal disk and placed between a spherical mirror M1 and a flat mirror M2. A piezoelectric actuator is affixed to the back mirror. The incoming IR laser beam is sent into the optical cavity containing the membrane in a Membrane at the Edge (MATE) geometry, and an FPGA is used to detect the transmitted light and lock the cavity.

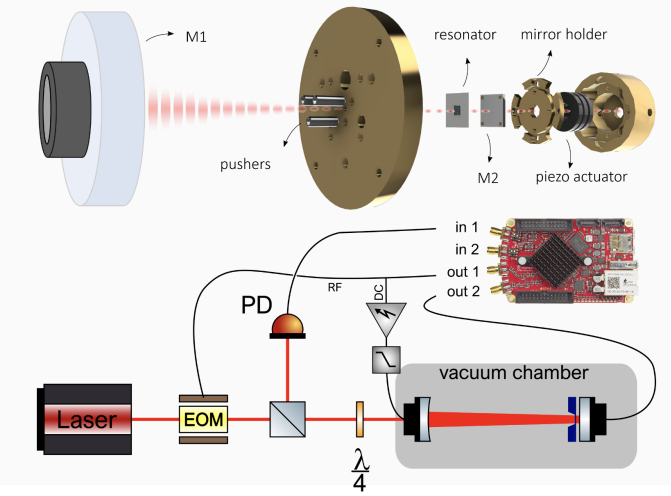

FIG. 25: LKB's Membrane Experiment [14].

B. Square Membrane Ring Down

First, preliminary tests were performed on a simple SiN square membrane, an example of which is shown in Figure 26 on the following page.

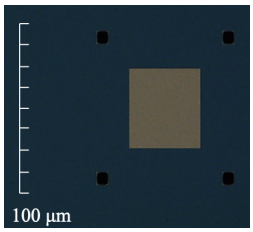

FIG. 26: Square Membrane Image Under Microscope.

A square membrane's mechanical modes upon excitation at different frequencies are shown in Figure 27 below.

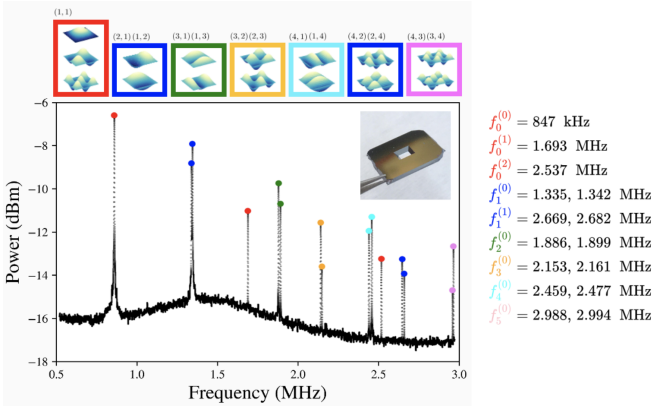

FIG. 27: Mechanical Modes of Square Membrane [14].

We performed a ring down of the square membrane at room temperature and atmospheric pressure (no vacuum chamber yet). A ring down is where light is injected onto a membrane and the power of the reflected light is measured. This test shows the resonator lifetime—how long the membrane sustains vibrations—and is used to ascertain the membrane's mechanical Q factor. The Q factor is a measure of the damping of a resonator's oscillations. A high Q factor indicates that membrane oscillations are minimally damped, so the membrane vibrates for a long time. In contrast, a low Q factor indicates that membrane oscillations are highly damped, so die out quickly. The Q factor depends on the membrane design and the particular mechanical mode that is excited [21].

In a ring down, light power changes with time according to an exponential decay $f(t) = e^{-\gamma_m t}$. When graphed in log scale, this becomes $g(t) = 1 - \gamma_m t$, a linear equation where the slope m represents the exponential decay factor γ_m. Nine square membrane ring downs were performed and graphed, their linear fits determined, and the average linear fit graphed in black in Figure 28 to the right.

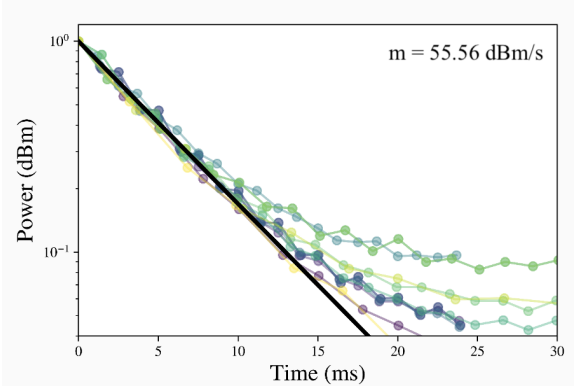

FIG. 28: Reflected Power vs Time During Ring Down of Square Membrane.

Knowing γ_m as well as the fundamental mechanical mode of oscillation ($f_0 = 847$ KHz), we can calculate the membrane's Q factor using 16 below [25].

$$Q = \frac{\omega_m}{\gamma_m} = \frac{2\pi f_0}{\gamma_m} \tag{16}$$

$$= \frac{2\pi(847 \times 10^3)}{55.56} \tag{17}$$

$$= 95,793 = 9.5793 \times 10^4 \tag{18}$$

Reetz et al. and other optomechanics experiments have obtained Q factors of SiN membranes via ring down ranging from about 3×10^5 to 10^6 under room temperature. These values significantly exceed our measured Q factor because they were obtained under vacuum. This demonstrates to what extent the introduction of vacuum improves the Q factor of membrane resonators. In both vacuum and cryostat environments, LKB's ultimate experimental goal, Q factors are even higher; Q reaches 6×10^7 under 4K [25].

C. Phononic Crystal Membrane Design and Fabrication

After sufficiently testing square membranes, LKB will begin testing phononic crystal membranes. What is advantageous about phononic crystal membranes is that they have a mechanical bandgap. This allows for oscillations at a single target frequency, reducing parasitic mechanical modes. The Q factor of this target mode is therefore very high. Secondly, oscillations are isolated in the membrane's central defect. With square membranes, dissipation of mechanical motion occurs through bending at the clamping points. But when oscillations are isolated at the center, the membrane edges do not move, which allows for what is called soft phononic clamping. This means there are fewer losses and longer oscillation lifetimes, sometimes lasting over 100 seconds [28].

The current phononic crystal membrane designs being fabricated and tested at LKB are the "Lotus" and

"Dahlia" designs shown in Figure 29 below.

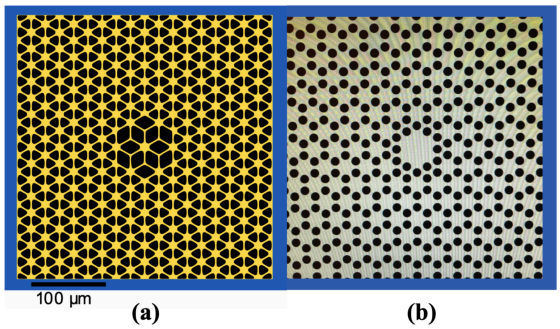

FIG. 29: The (a) Lotus and (b) Dahlia Phononic Crystal Membrane Designs.

Membranes are 1 mm by 1 mm and must be designed with a central defect diameter of $6w_0$ to ensure that the Gaussian beam hits *only* the defect, as shown in Figure 30 below. The same MATE cavity geometry is used with spherical mirror M1 of radius of curvature R, flat mirror M2, and cavity length L.

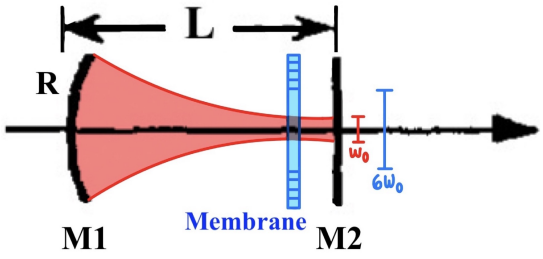

FIG. 30: Side View of Gaussian Beam Hitting Membrane with Defect Diameter of $6\omega_0$ in MATE Cavity Geometry. Adapted from [16].

Diameters of the defect were calculated using Equation 19, which gives the beam waist in this particular cavity geometry as a function of R and L [16]. An input IR beam of wavelength $\lambda = 1064$ nm is used to probe the membranes.

$$\omega_0(R, L) = \sqrt{\frac{\lambda}{\pi}\sqrt{L(R-L)}} \tag{19}$$

LKB will test three different cavity sizes, which each require a membrane defect of a slightly different diameter, as shown in Table I to the right.

	R	L	Defect Diameter = $6\omega_0$
Membrane 1	25 mm	1.7 cm	377 μm
Membrane 2	15 mm	14 mm	214 μm
Membrane 3	10 mm	9 mm	191 μm

TABLE I: Membrane Defect Diameter for Three Cavity Sizes of Interest.

Membrane fabrication involves a multistep lithography process in the clean room, beginning with a thin wafer of silicon (Si) coated on both sides with a thinner layer of silicon nitride (SiN). A membrane mask created using Python package DrawPy, as shown in Figure 31 below, is used to pattern the top SiN surface. The yellow refers to the fully intact SiN-Si-SiN, the blue partitions are the exposed Si surfaces where cleaving will occur, and the magenta squares are the membranes, consisting of only the top SiN layer with holes arranged in either the Lotus or Dahlia pattern.

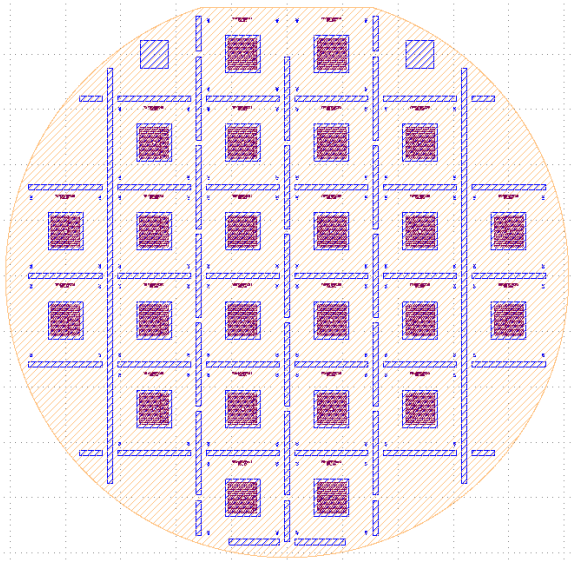

FIG. 31: A 5 cm x 5 cm Membrane Mask Design Containing 24 Membranes of 1 mm x 1 mm.

The wafer's top SiN surface is first treated with a layer of photoresist which, when exposed to UV light, becomes soluble in a developer. A lithography machine shines a UV laser on this surface following the pattern of the mask. The wafer then soaks in the developer, which dissolves some of the photoresist, resulting in a partially exposed SiN surface according to the membrane pattern. A Reactive Ion Etching (RIE) machine then exposes the wafer to plasma that reacts only with SiN, etching all the way down to the Si layer, thus creating the thin SiN membranes. The wafer's back SiN layer is then patterned with a grid of squares that are each aligned with a membrane on the front side. The back side is exposed to potassium hydroxide, which etches a pyramid in the Si from the back to the front side, creating a chocolate bar-

esque pattern of partitions around each SiN membrane allowing for them to be cleaved from the Si base. The cleaving process is still being optimized at LKB to allow for the highest yield of unbroken membranes.

V. FUTURE WORK AND APPLICATIONS

Advancements to this experiment include testing square membranes under vacuum and then testing phononic crystal membranes at atmospheric pressure and under vacuum. We aim to test both the Dahlia and Lotus designs, comparing their ease of fabrication, Q factors, mechanical bandgaps, and other properties to ascertain which design has the best optomechanical performance. Finally, there is LKB's ultimate goal of testing phononic crystal membranes under vacuum, in a cryostat, and with FDSL.

Inputting FDSL into these membrane cavities accomplishes the same thing as in gravitational wave interferometers: it compensates for the dominance in noise that occurs around resonant frequencies. It is yet another demonstration that it is possible to beat the Standard Quantum Limit. The only difference is that resonance for the membranes occurs in middle-frequency ranges, around 1-2 MHz, whereas for GW detectors, resonance is much lower, around 1-10 Hz [17].

Phononic crystal membranes have numerous applications in squeezed light experiments, quantum informatics, and microscopy. Coupling between mechanical membrane resonators and superconducting "fluxonium" qubits is a promising way to build scalable quantum computers. Long oscillation lifetimes of the membranes mean long coherence times: more time over which quantum information is stored. These qubits also provide ways to test theories of gravity quantization [22]. Finally, scanning force microscopy is achievable with SiN membrane optomechanical coupling. The standard microscope geometry can be inverted: samples are placed on a vibrating membrane surface and the scanning tip is at rest [12].

VI. CONCLUSIONS

This summer, I aided in the optimization of two optics experiments at Laboratoire Kastler-Brossel: a frequency-dependent squeezed light generator and a membrane optomechanics experiment. Understanding the quantum nature of light and the interaction between light and mechanical motion is crucial in improving gravitational wave detectors, quantum computers, and microscopy.

In the squeezed light generator, the SHG was aligned, mode matched, and locked and its conversion efficiency was optimized to 54.3%. Devices were designed to improve the crystal positioning in the SHG and OPO in order to ease mode matching. Future work involves mode matching and optimizing the OPO, mode cleaner, and filter cavity before making a final measurement of FDSL, which we expect to be an improvement from LKB's previous squeezer. Calculations must also be done to derive the optimal squeezing angle for each light frequency for use in the membrane experiment.

In the membrane experiment, a Q factor of 56,793 was obtained for a square SiN membrane at room temperature and atmospheric pressure. Two phononic crystal membrane designs—the Lotus and Dahlia—were finalized and the first wafers were fabricated in the clean room. Future work involves testing phononic crystal membranes in cavities of various sizes at atmospheric pressure and under vacuum, comparing the two designs to determine the optimal design for the final cryogenic optomechanics experiment.

VII. ACKNOWLEDGEMENTS

I would like to thank the Optomechanics and Quantum Measurements Group at LKB for this incredible summer opportunity. Specifically, I'd like to thank PhD student Pierre-Édouard Jacquet and PI Dr. Pierre-François Cohadon for mentoring me. PhD students Émile Ferreux and Himanshu Patange, Master's student Paul Manset, and PIs Dr. Samuel Deléglise and Dr. Tristan Briant were also incredible, welcoming mentors. I would like to thank UF professors Dr. Paul Fulda, Dr. Peter Wass, and Dr. Kathryn McGill for selecting me for this unique program, organizing my housing, and providing ongoing academic and moral support. Thank you too to Faustine Giraud, my fellow summer intern at LKB, and to my IREU cohort full of amazing individuals who I stayed in contact with, visited, and learned from throughout these two months. Finally, this wouldn't have been possible without the National Science Foundation's PHY-1950830 grant which provided funding for my flights, housing, and summer stipend.

[1] Barriga, P., Blair, D., Coward, D., Davidson, J., Dumas, J.-C., Howell, E., Ju, L., Wen, L., Zhao, C., McClelland, D., Scott, S., Slagmolen, B., Hosken, D., Munch, J., Ottaway, D., Veitch, P., Melatos, A., Chung, C., Sammut, L., & Sathyaprakash, B. (2013). AIGO: A Southern Hemisphere Detector for the Worldwide Array of Ground-Based Interferometric Gravitational Wave Detectors. *Classical and Quantum Gravity.*

https://doi.org/10.1088/0264-9381/27/8/084005.

[2] Bitarafan, M., & DeCorby, R. (2017). On-Chip High-Finesse Fabry-Perot Microcavities for Optical Sensing and Quantum Information. *Sensors*, 17(8), 1748. https://doi.org/10.3390/s17081748.

[3] Caves, C. M., & Schumaker, B. L. (1985). New Formalism for Two-Photon Quantum Optics. I. Quadrature Phases and Squeezed States. *Physical Review A*, 31(5), 3068–3092. https://doi.org/10.1103/PhysRevA.31.3068.

[4] Chelkowski, S., Vahlbruch, H., Hage, B., Franzen, A., Lastzka, N., Danzmann, K., & Schnabel, R. (2005). Experimental Characterization of Frequency-Dependent Squeezed Light. *Physical Review A*, 71(1), 013806. https://doi.org/10.1103/PhysRevA.71.013806.

[5] Chua, S. S. Y. (2013). Quantum Enhancement of a 4 km Laser Interferometer Gravitational-Wave Detector. *Springer International Publishing*. https://doi.org/10.1007/978-3-319-17686-4.

[6] Chua, S. S. Y., Slagmolen, B. J. J., Shaddock, D. A., & McClelland, D. E. (2014). Quantum Squeezed Light in Gravitational-Wave Detectors. *Classical and Quantum Gravity*, 31(18), 183001. https://doi.org/10.1088/0264-9381/31/18/183001.

[7] Cohadon, P.-F., Heidmann, A. (2021). Early History and Fundamentals of Optomechanics. *Quantum Optomechanics and Nanomechanics*, 1-40. https://doi.org/10.1093/oso/9780198828143.003.0001.

[8] Columbia Engineering. (n.d.). Section 2.7: TEM Mode, Beam Diameter. *Advanced Manufacturing Laboratory*. Retrieved August 2, 2023, from http://www.aml.engineering.columbia.edu/ntm/level2/ch02/html/l2c02s07.html.

[9] Croquette, M. (2022). Optomécanique et Lumière Comprimée. *Sorbonne Université*. https://www.theses.fr/2022SORUS473.

[10] Dumont, V., Bernard, S., Reinhardt, C., Kato, A., Ruf, M., Sankey, J. C.. (2019). Flexure-Tuned Membrane-at-the-Edge. *Optomechanical System*, 27(18), 25731-25748. https://doi.org/10.1364/OE.27.025731.

[11] Elmadih, W., Syam, W. P., Maskery, I., Chronopoulos, D., & Leach, R. (2019). Mechanical Vibration Bandgaps in Surface-Based Lattices. *Additive Manufacturing*, 25, 421–429. https://doi.org/10.1016/j.addma.2018.11.011.

[12] Hälg, D., Gisler, T., Tsaturyan, Y., Catalini, L., Grob, U., Krass, M.-D., Héritier, M., Mattiat, H., Thamm, A.-K., Schirhagl, R., Langman, E. C., Schliesser, A., Degen, C. L., & Eichler, A. (2021). Membrane-Based Scanning Force Microscopy. *Physical Review Applied*, 15(2), L021001. https://doi.org/10.1103/PhysRevApplied.15.L021001.

[13] InfiniQuant. (n.d.). Tutorial: Continuous-Variable Quantum Communication. *InfiniQuant*. http://infiniquant.com.

[14] Jacquet, P.-E., Croquette, M., Chua, S., Deléglise, S., Cohadon, P.-F..(2023). Frequency-Dependent Squeezing for Optomechanics Experiments [PhD Seminar]. Laboratoire Kastler-Brossel, Sorbonne Université Pierre et Marie Curie.

[15] Junker, J., Wilken, D., Johny, N., Steinmeyer, D., & Heurs, M. (2022). Frequency-Dependent Squeezing from a Detuned Squeezer. *Physical Review Letters*, 129(3), 033602. https://doi.org/10.1103/PhysRevLett.129.033602.

[16] Kogelnik, H., Li, T. (1966). "Laser Beams and Resonators" *Applied Optics*, 5 (10), 1550-1567. https://doi.org/10.1364/AO.5.001550.

[17] LIGO. (n.d.). LIGO's Interferometer. *LIGO Caltech*. Retrieved August 2, 2023, from https://www.ligo.caltech.edu/page/ligos-ifo.

[18] Ling, J. S. (2020). Fabry-Perot Interferometer. Retrieved August 2, 2023, from http://www.physicsbootcamp.org/section-fabry-perot-interferometer.html.

[19] McCuller, L., Whittle, C., Ganapathy, D., Komori, K., Tse, M., Fernandez-Galiana, A., Barsotti, L., Fritschel, P., MacInnis, M., Matichard, F., Mason, K., Mavalvala, N., Mittleman, R., Yu, H., Zucker, M. E., & Evans, M. (2020). Frequency-Dependent Squeezing for Advanced LIGO. *Physical Review Letters*, 124(17), 171102. https://doi.org/10.1103/PhysRevLett.124.171102.

[20] Neuhaus, L. (2017). Cooling a Macroscopic Mechanical Oscillator Close to its Quantum Ground State. *HAL Thèses en Ligne*. https://theses.hal.science/tel-01467924v2.

[21] Neuhaus, L., Croquette, M., Chua, S., Jacquet, P.-E., Cohadon, P.-F., Heidmann, A., & Deleglise, S. (2023). FPGA-Based Feedback Control of Quantum Optics Experiments with the Open Source Software Package PyRPL.

[22] Najera-Santos, B.-L., Rousseau, R., Gerashchenko, K., Patange, H., Riva, A., Villiers, M., Briant, T., Cohadon, P.-F., Heidmann, A., & Palomo, J. (2023). High-Sensitivity AC-Charge Detection With a MHz-Frequency Fluxonium Qubit. *HAL Science*, https://hal.science/hal-04169999/document.

[23] Optique Ingénieur. (n.d.). Optical Resonators and Gaussian Beams—Hermite-Gaussian Modes. *OPI Online Courses*. Retrieved August 2, 2023, from http://www.optique-ingenieur.org/en/courses/OPI_ang_M01_C03/co/Contenu_13.html.

[24] Page, M. A., Goryachev, M., Miao, H., Chen, Y., Ma, Y., Mason, D., Rossi, M., Blair, C. D., Ju, L., Blair, D. G., Schliesser, A., Tobar, M. E., & Zhao, C. (2021). Gravitational Wave Detectors with Broadband High-Frequency Sensitivity. *Communications Physics*, 4(1), 27. https://doi.org/10.1038/s42005-021-00526-2.

[25] Reetz, C., Fischer, R., Assumpção, G. G. T., McNally, D. P., Burns, P. S., Sankey, J. C., & Regal, C. A. (2019). Analysis of Membrane Phononic Crystals with Wide Band Gaps and Low-Mass Defects. *Physical Review Applied*, 12(4), 044027. https://doi.org/10.1103/PhysRevApplied.12.044027.

[26] Schnabel, R. (2017). Squeezed States of Light and Their Applications in Laser Interferometers. *Physics Reports*, 684, 1–51. https://doi.org/10.1016/j.physrep.2017.04.001.

[27] Schreppler, S., Spethmann, N., Brahms, N., Botter, T., Barrios, M., & Stamper-Kurn, D. (2014). Optically Measuring Force Near the Standard Quantum Limit. *Science*, 344(6191), 1486-1489. https://doi.org/10.1126/science.1249850.

[28] Tsaturyan, Y., Barg, A., & Polzik, E. (2017). Ultracoherent Nanomechanical Resonators via Soft Clamping and Dissipation Dilution. *Nature Nanotech*, 12, 776–783. https://doi.org/10.1038/nnano.2017.101.